Hydrogen trapping by irradiation-induced defects in 316 Lstainless steel: A combined experimental and modeling study

Anne-Cécile Bach, Frantz Martin, Cecilie Duhamel, Stéphane Perrin, François Jomard, Jérôme Crépin

Version of Record: https://www.sciencedirect.com/science/article/pii/S002231152200099X
Manuscript_5119502fbe961820bd1c85e5455ee590

HYDROGEN TRAPPING BY IRRADIATION-INDUCED DEFECTS IN 316L STAINLESS STEEL: A COMBINED EXPERIMENTAL AND MODELLING STUDY

Anne-Cécile BACH [1], [2], Frantz MARTIN [1], Cécilie DUHAMEL [2], Stéphane PERRIN [3], François JOMARD [4], Jérôme CREPIN [2]

[1] Université Paris-Saclay, CEA, Service de la Corrosion et du Comportement des Matériaux dans leur Environnement, 91191, Gif-sur-Yvette, France

[2] MINES ParisTech, PSL University, MAT- Centre des matériaux, CNRS UMR 7633, BP 87, 91003 Evry, France

[3] CEA, DES, ISEC, DE2D, SEAD, LCBC, Univ Montpellier, Marcoule, France

[4] Groupe d'Etude de la Matière Condensée, CNRS, UVSQ, 45 avenue des Etats-Unis, 78035 Versailles cedex, France

Abstract:

The irradiation-induced defects in stainless steel internal components of pressurized water reactors combined with hydrogen uptake during the oxidation process could be a key parameter in the mechanism for Irradiation-Assisted Stress Corrosion Cracking (IASCC). A heat-treated 316L SS containing a low amount of defects was Fe^{3+} ions-implanted; irradiation-induced defects types and depth distributions were characterized by Transmission Electron Microscopy (TEM). Deuterium was then inserted in the specimens either by cathodic charging or by sample exposure to deuterated primary water. Secondary Ions Mass Spectrometry – SIMS – permitted to access the deuterium distribution at the implanted stainless steel surface. A finite difference numerical solver accounting for hydrogen diffusion/trapping coupling was used to simulate the hydrogen transport in the implanted material, taken into consideration the specific heterogeneous character of the irradiation-induced defects distribution in matter. Taking as input data the experimental defects distribution associated with Frank loops or voids, the main trapping sites for hydrogen were assigned to voids, not Frank loops. Such numerical approach was able to deal accurately with the problem of hydrogen transport in a heterogeneous material as well as to differentiate two potential trap sites contributions to the experimental deuterium distribution. In addition, according to results obtained after primary water exposure, trapping at voids was still effective at 320 °C, signature of a high binding energy of hydrogen in voids.

Keywords:

Hydrogen trapping, Irradiation defects, Austenitic stainless steel, Secondary Ions Mass Spectrometry, Modelling

1. INTRODUCTION

Austenitic stainless steels are currently used for several structural components of Light Water Reactors (LWR) such as the vessel internals and the associated baffles and bolts in the reactor core. In Pressurized Water Reactor (PWR), austenitic stainless steels (SS) are exposed to primary water, which is basically an aqueous solution containing dissolved hydrogen (in the 5 – 50 cm^3 H_2 / kg H_2O NTP range) at a temperature ranging between 290 °C and 325 °C and a pressure of about 155 bar. Beyond the joint action of this corrosive environment and mechanical and thermal stresses applied to the SS structural components, which can lead to stress corrosion cracking (SCC), an additional external factor has to be considered in the reactor core: the neutron flux emitted by the nuclear fuel. Since the eighties, some cracks have been observed on SS baffles and bolts in the reactor core. They could result from a phenomenon denoted Irradiation-Assisted Stress Corrosion Cracking (IASCC) although all the mechanisms are not totally understood yet [1,2].

Although the effect of hydrogen altering mechanical properties of carbon steels and stainless steels at temperature below 150 °C [3-5] is well documented, its potential role in the mechanisms of crack initiation and propagation during SCC or IASCC is generally neglected due to the high temperature at which these phenomena occur in PWRs. Indeed, Chêne *et al.* showed that under hydrogen equivalent overpressures possibly encountered in primary water (around 0.2 to 4 bar) [6], hydrogen trapping at defects such as dislocations would be very low for such nominal conditions, therefore discarding potentially any implication of hydrogen effect on local plasticity modification as classically referred to in hydrogen embrittlement mechanisms [5, 7-10]. However it has recently been estimated that during the corrosion process, especially at the very first steps of passivation, the equivalent partial pressure seen by the alloy could reach 15 bar [11], challenging this view point on hydrogen participation to SCC propagation mechanisms. Direct hydrogen implication in SCC, and consequently in IASCC mechanisms is still not a consensus, even though several studies made on nickel-base alloys [12,13] or stainless steels [14] in primary water showed an effect of dissolved hydrogen on crack initiation and propagation during SCC. Zhong *et al.* [14] studied a 316 stainless steel using slow strain rate tests in simulated PWR primary water. They highlighted the possible mitigation of the crack initiation by increasing the dissolved hydrogen level as well as a maximum in the crack growth rate at a dissolved hydrogen content of about 15 cm^3 (NTP) H_2 / kg H_2O. Rios *et al.* [13] found the same behavior for the

crack growth rate in Alloy 600, on reverse U-bends, reaching a maximum for an intermediate hydrogen overpressure (4 bar). Their works highlight a strong effect of hydrogen overpressure in contrast with a non-hydrogenated media on the time-to-failure and detected crack length. Nevertheless, the nature of the effects of hydrogen in the SCC mechanisms is not clearly determined yet. The information available in literature indicates however that some hydrogen is absorbed in the alloy during PWR corrosion process. Indeed, Dumerval *et al*. [15] highlighted, thanks to the GD-OES (Glow discharge Optical Emission Spectroscopy) technique, that a non-negligible amount of hydrogen was incorporated and trapped in the alloy beneath the oxide/alloy interface during exposure of 316L SS to simulated PWR primary water. Primary water is actually a huge source of hydrogen (be it the water molecules or dissolved hydrogen) which can dissociate at the surface, for instance during the oxidation process (cathodic reaction), then diffuse through the oxide layer and in the alloy and interact with structural defects where it could eventually be trapped. As an illustration, in Dumerval's work [15], the accumulation of hydrogen just below the oxide/alloy interface for the 316L SS was assigned to trapping at vacancies that were created by the cationic-grown part of the oxide layer. Such hydrogen trapping at temperatures as high as those found in PWR primary water implies, as previously suggested for dislocations due to local high equivalent partial pressure, a possible local accumulation of hydrogen in the process zone of a crack tip, eventually helping crack propagation.

During in-core nuclear power plant exposure conditions, interactions of neutrons with the alloy atoms induce the creation of structural defects such as vacancies, interstitials, voids (or cavities), He bubbles, black dots, dislocation loops…[16-20]. All these defects could be additional trapping sites for hydrogen, and participate directly or indirectly to the premature failure of the components exposed to the primary water in the reactor core. Many authors studied hydrogen trapping or interactions with irradiation-induced defects in fcc alloys, mostly by direct implantation of protons or deutons. They showed that irradiation-induced dislocations could trap hydrogen in the 300-450 K range, and that irradiation-induced He or Ar bubbles constitute the most efficient traps for hydrogen [21-25]. Besides, Karpov *et al*. [23] state that dislocation loops do not modify hydrogen transport in the material, and suggest that main traps for hydrogen in irradiated fcc materials are vacancies. Garner *et al*. [26] reported that hydrogen levels in neutron irradiated cold-worked 316 stainless steel in the 400-550 °C range could be as high as 500 at.ppm : no direct correlation with the dislocation structure, total void voume nor void surface area could be clearly established. In any case, no direct link between local density of irradiation-induced defects and hydrogen localization was made, especially on non-hydrogen implanted specimen: all these conclusions are indeed deduced from global analysis such as thermal desorption spectrometry and general defect size and/or type characterization evolution with temperature or irradiation time. One of the aims of the present paper is to tackle this link.

The main difficulty in studying hydrogen uptake during PWR in core exposure stands in the activation of materials under neutron flux that renders analysis much more complex than a 'simple' autoclave

exposure. For this reason, a way to cover both effects (irradiation and corrosion of SS in primary water) is to separate each effect in a segmented way and work with these elementary blocks. Thus, alternating irradiation and environmental exposure sequentially would render the synergetic interaction of irradiation and corrosion occurring in the reactor core. For comprehension reasons, a comparison with a reference material is always necessary.

To simulate neutron irradiation defects while avoiding difficulties of neutron irradiation experiments (time, cost, activation…), ion implantation of light or heavy ions are often used, provided some conditions are respected. In order to compensate the much higher dose rate induced by ion irradiation, compared to neutron irradiation, ion irradiation must be carried out at high temperature to favor defects recombinations [27]. Light ion implantation, like protons, leads to the formation of dislocation loops with a density and a mean size in the same order of magnitude that those created by neutrons irradiation, as shown by Was *et al.* [27,28]. Moreover proton implantation of stainless steels reproduces grain boundary microchemistry (radiation-induced segregation) and radiation-induced hardening that are representative of neutron-irradiated materials. However, during proton implantation, hydrogen is uptaken by the material at the very same time as irradiation defects are created. This simultaneity, even if representative of some reality in terms of potential proton irradiation in core, may ease the creation of alternative defects, such as hydrogen-vacancy clusters, that would not be present otherwise [29] and not fully representative of interactions of hydrogen coming from the corrosion reactions, inserted in the material in interstitial sites, with irradiation defects. In addition, relevant damage and damage rate is hardly reached with proton implantations. Heavy ion implantations are therefore sometimes used. They allow the creation of a lot of damages within a short period of time at the expense of a much smaller penetration depth (1-2 µm) as compared to those affected by neutron irradiation. The implanted microstructure presents the same type of defects (dislocation loops and cavities) as neutron-irradiated material, and, if the implantation conditions are well mastered, representative defect types and distributions can be achieved [27,30-36].

As possible hydrogen trap sites in austenitic stainless steels present in reactor core are numerous (dislocations, vacancies, irradiation defects …), the focus was made in the present study on specific defects associated only with irradiation. A sequential approach based on ion implantation in a reference material (with the fewest possible defects), defects characterization by TEM, followed by hydrogen exposure and hydrogen distribution study was chosen as a first step towards a thorough characterization of hydrogen-irradiation defects interactions in austenitic stainless steels during in-core exposure. Despite some differences with neutron-induced defects, iron ion implantation was chosen to create defects with quite similar nature and relevant in terms of density and size to start to investigate the interactions between hydrogen and irradiation defects [31,34-36]. Iron ions also allowed to minimize the modifications induced by implantation on the average alloy composition (iron being the main element).

The aim of this study is to highlight the hydrogen trapping related to implantation-induced defects and thus to characterize the interactions between hydrogen and these defects thanks to numerical simulations. For that, deuterium was used as a hydrogen isotopic tracer. The deuterium uptake was promoted in the 316L SS by room temperature cathodic charging and deuterium distribution profiles were analyzed by SIMS depth profiles. In addition, original numerical calculations were performed, solving the hydrogen diffusion/trapping in a non-homogeneous matrix involving a depth-dependent trap site density linked to the experimentally-determined irradiation-induced defects distribution. It allowed to adequately analyze the experimental deuterium distribution in the alloy (from SIMS profiles) with respect to the defect density profiles experimentally determined by TEM image analysis. Finally, the trapping ability of implantation-induced defects in PWR primary water conditions was investigated by exposing some implanted specimens to simulated primary heavy water.

2. MATERIALS AND METHODS

2.1. Materials

2.1.1. Reference material

An industrial grade of 316L SS was used in this study. Its chemical composition is given in Table 1. Large samples (110 mm x 22 mm x 1.5 mm) were cut by electrical discharge machining and then polished with grade 1200 SiC paper. A first thermal treatment of 1 hour at 1080 °C under an argon overpressure, followed by oil quenching, was performed to annihilate dislocations and dissolve carbides potentially initially present in the as-received material. Then a second heat treatment of 15 hours at 300 °C was imposed to evacuate thermal vacancies possibly retained in the alloy during quenching as well as to relax residual stresses due to quenching. The two thermal treatments aimed at elaborating a reference material containing a minimum quantity of defects. Coupons of 20 mm x 20 mm x 1.5 mm were then cut with a low-speed precision cut-off machine, to minimize the creation of new defects (dislocations mainly), and ground with SiC paper down to grade 2000, polished with diamond paste down to 3 µm, followed by a mirror finish on a vibratory table with a colloidal silica suspension. The as-prepared samples will be called “reference material” thereafter. As ion implantations were performed at 500 °C (see next section), an additional heat treatment, i.e. 1 h at 500 °C in vacuum, was carried out on some of these reference material coupons to simulate the thermal history of ion-implanted samples. This set of samples will hereafter be referred to as “heat-treated reference specimens”.

Table 1 : Nominal composition of the industrial 316L SS in wt.% obtained by Optical Emission Spectrometry.

	Nominal	Measurement uncertainty
C	0.019	± 0.003
Si	0.33	± 0.01
Mn	1.33	± 0.02
S	< 0.003	-
P	0.025	± 0.003
Ni	10.36	± 0.15
Cr	16.94	± 0.15
Ti	0.024	± 0.003
Co	0.10	± 0.01
Al	< 0.01	-
Cu	0.23	± 0.01
Mo	2.08	± 0.03
Fe	Bal.	-

2.1.2. Implanted material

5 MeV Fe^{3+} ion implantations were performed on some reference material specimens at JANNuS-Saclay (Joint Accelerators for Nanoscience and Nuclear Simulation), CEA, France, to create sub-surface defects. An implantation temperature of 500 °C was used, in order to compensate the effect of higher dose rate with ion irradiation on microstructural evolution. Two series of implantations were performed, thereafter referred to as JANNuS#1 and JANNuS#2 respectively. JANNuS#1 implantation was done in a triple beam chamber – using only a single 15° incident beam –, with a total dose ranging between 3 x 10^{15} at.cm^{-2} and 8 x 10^{15} at.cm^{-2} and so an average value of 5.5 ± 2.5 x 10^{15} at.cm^{-2} and a mean flux of 1.2 ± 0.5 x 10^{12} at.cm^{-2}.s^{-1}. The uncertainties are due to a technical problem of dose measurement during implantations.; JANNuS#2 specimen were implanted in a single beam chamber – 0° incident beam –, with a total dose ranging between 3 x 10^{15} at.cm^{-2} and 4 x 10^{15} at.cm^{-2} (average value of 3.5 ± 0.5 x 10^{15} at.cm^{-2}) and a mean flux of 6.2 ± 0.9 x 10^{11} at.cm^{-2}.s^{-1}. Each implantation run lasted around 1 hour (isothermal, in flux duration). Using SRIM Monte Carlo simulation code as detailed in Stoller's work [37], theoretical damages induced by implantation were estimated, under the Kinchin-Pease approximation, in dpa (displacement per atom). Implantation conditions were chosen so that the implantation peak was located in the volume, but not too far from the surface in order to optimize further analyses. With our implantation conditions, the calculated mean damages reached up ~ 6 ± 2 dpa and ~ 4 ± 0.5 dpa at ~ 1.3 µm depth for JANNuS#1 and JANNuS#2 respectively, as shown in Figure 1.

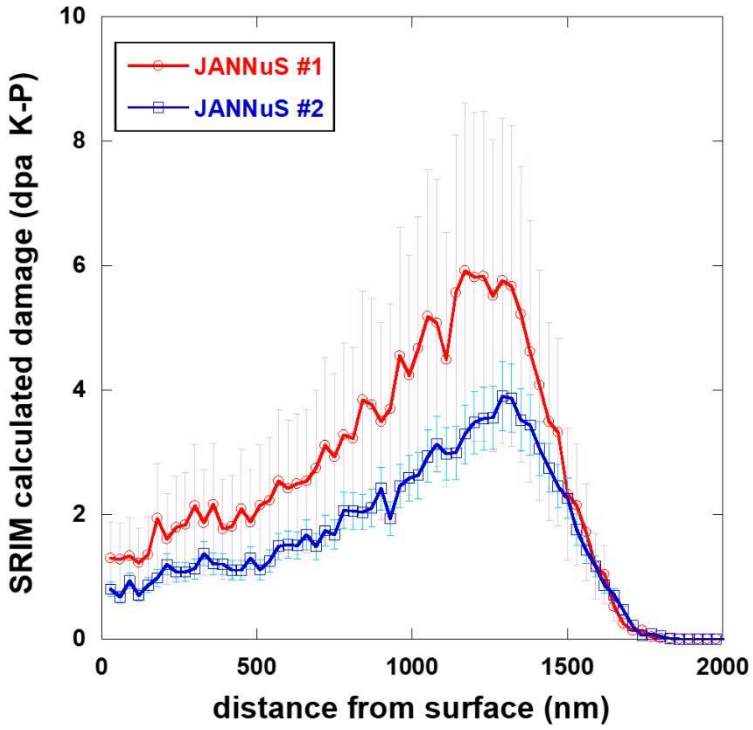

Figure 1 : SRIM cumulated mean damage (dpa) simulation for JANNuS#1 (red circles) and JANNuS#2 (blue squares) implantation conditions. The error bars show scattering due to flux measures uncertainties.

Five Faraday cups were used in the specimen chamber to monitor the irradiation beam current. It was checked at every 10 min to extrapolate the actual value of implantation dose. The irradiation temperature was controlled by one thermocouple in the sample support and monitored by an IR camera. The setpoint temperature had to be reduced at the beginning of the experiment to compensate for implantation-induced heating.

2.2. Transmission Electron Microscopy (TEM)

Transmission electron microscopy (TEM) observations were carried out using a FEI TECNAI F20-ST field emission gun microscope operated at 200 kV. For the reference material, thin foils were prepared by twin jet electrolytic thinning at 0°C and a voltage of 30V in a solution made of 45% butoxyethanol, 45% acetic acid and 10% perchloric acid (volume fractions). For the ion-implanted samples, focused ion beam (FIB) was used to prepare TEM specimens in order to characterize the density and size distributions of the implantation-induced defects in depth from the surface. The Frank loops were imaged in dark-field conditions using the rel-rod technique [17]. Frank loops are faulted dislocation loops lying in {111} planes with a Burger vector **a**/3<111>, i.e. four variants of loops exist. Only two

of them were characterized in present study. The total loop density was calculated assuming that the Frank loop population is similar in the four {111} planes of the face-centred cubic (fcc) structure. The cavities were imaged out of contrast in bright-field conditions where they appear either as white discs surrounded by a dark fringe (under-focus) or as dark discs circled by a white fringe (over-focus). In this way, one is sure that the round defects observed are cavities and not precipitates or black dots for instance. The thickness of the TEM specimens was assumed equal to 100 $\pm$ 10 nm.

In order to check that FIB preparation did not introduce defects in the material similar to those created by ion implantation, TEM observations in the conditions described above were made on the non-implanted zone of the thin foil. These examinations did not reveal the presence of dislocation loops nor cavities, suggesting that potential damage induced by FIB preparation would not alter the obtained results.

2.3. Cathodic charging

In order to study the interactions between implantation-induced defects and hydrogen, deuterium was introduced in both the heat-treated reference and implanted samples by cathodic charging at 25 °C in a deaerated (Ar bubbling) 0.1 M NaOD solution made by dissolving solid soda pellets in 99.96 % deuterium-containing heavy water. A galvanostat was used to impose a constant current density between the working electrode (specimen) and a Pt grid counter electrode throughout the hydrogen charging procedure duration. The value of the imposed cathodic current density *j,* of -1 mA.cm^{-2}, was chosen to maximize hydrogen adsorption (then absorption in the specimen) on the surface from the proton reduction within the Volmer-Tafel electrochemical domain of the cathodic branch. The duration of the cathodic charging of 3 hours was estimated thanks to preliminary rough calculations so that the implanted zone of the specimens was charged enough, for potential trapping to occur, but also so that diffusion inwards the bulk was not widespread too far from the surface.

Directly after cathodic charging, samples were quickly transferred and stored in liquid nitrogen (77 K) in order to prevent deuterium desorption (effusion) and block further internal diffusion.

2.4. Aging

After deuterium cathodic charging of fcc materials containing low trap densities, the main contribution to the deuterium concentration profile is generally due to interstitial deuterium atoms, that hinder the trapped deuterium concentration profile. In order to increase all chances to highlight potential deuterium trapping at defects formed in the implanted zone of the samples, i.e. within the first 1600 nm, an additional aging step was performed. The aim was to enhance the trapped-to-interstitial deuterium atoms ratio in the implanted zone. Controlled desorption or retrapping under vacuum isothermal conditions had to be performed with both reasonable timescales and the least possible modifications of the defects structure and distribution.

The aging step was designed thanks to preliminary calculations, inspired by McNabb and Foster's coupled Fick diffusion and trapping-detrapping kinetics set of equations [38] and based on former works [39,40]. In contrast with to-date literature-existing works, a non-homogeneous trap sites density was used as input data in present work to simulate the 1-2 µm implantation-affected zone under the specimens' surface. Preliminary calculations used a step-like trap density function within the first 2 µm, set at zero in the bulk. The set of equations used for these simulations are explicitly detailed in part 3.3. Figure 2 illustrates this optimization procedure carried out with an arbitrary sigmoidal-shape trap distribution in the first 2 µm below the surface (see insert in Figure 2.a). The black line represents the total deuterium concentration profile that would be recorded during secondary ions mass spectrometry (SIMS) depth profiling as all deuterium atoms are detected by SIMS irrespective of their 'state' (interstitial or trapped). After charging for 3 hours at 25 °C, the main contribution to the hydrogen concentration profile is interstitial hydrogen (red squares) and trapped hydrogen (blue diamonds) is negligible. However, after aging for some time at an adequate temperature (here 24 h at 40 °C), the trapped hydrogen atoms have become the major contribution in the volume of interest, i.e. the implantation zone compared to interstitial hydrogen, the latter being still detected but deeper in the sample. Optimization of the aging time and temperature lead to aging conditions of 24 hours spent at 40 °C in vacuum. This tempering was applied to all specimens that were prior cathodically charged.

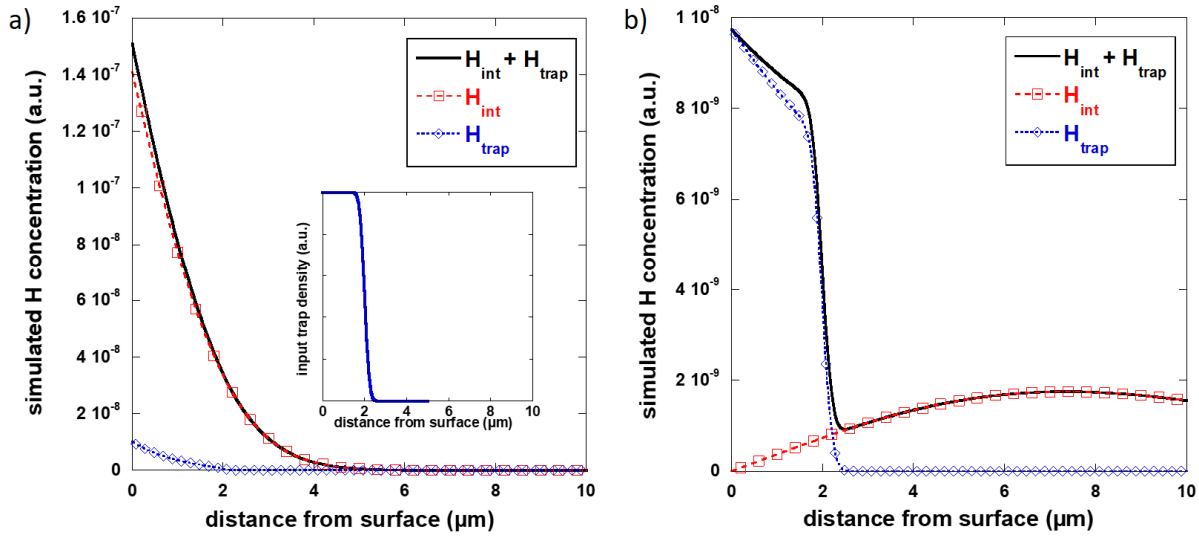

Figure 2 : Illustration of the preliminary calculations performed to optimize the charging – aging parameters necessary for enhanced detection of hydrogen atoms trapped by defects in the implanted zone (simulated by the input sigmoid function shown in the insert in a)). The total hydrogen (black curve), the interstitial hydrogen (red squares) and trapped hydrogen (blue diamonds) concentration profiles are represented a) just after charging for 3 hours at 25 °C, and b) after additional aging for 24 hours at 40 °C.

2.5. Exposure to simulated primary heavy water

Simulated primary water exposures were carried out in a static titanium (T40) 280 mL autoclave, for durations up to 500 hours. The use of Ti autoclave avoids potential contamination of the surface by metallic cations (Fe, Cr, Ni) coming from the autoclave during the test and that could artificially contribute to the surface oxide formation on the specimens. Three specimens, cut from the reference material, JANNuS#1 and JANNuS#2 implanted samples, were exposed to primary water. The medium used for the present study was heavy water (99.90 % of ^{2}H) containing 2 ppm Li (in the form of LiOH), 1000 ppm B (in the form of H_3BO_3) and 27 $cc.kg^{-1}_{D2O}$ (NPT) dissolved deuterium gas (100 % ^{2}H, brought by a Ar/4% $^{2}H_2$ gas mixture). The temperature was 320 °C, and the equilibrium pressure around 11.8 MPa (water/vapor equilibrium pressure). After the test, once the medium had cooled down to 40 °C, the samples were transferred directly and stored in liquid nitrogen, to avoid deuterium desorption at room temperature, waiting for further analysis.

2.6. SIMS analyses

SIMS (Secondary Ion Mass Spectrometry) analyses were conducted on both the heat-treated reference and the implanted samples after deuterium charging and aging, and after exposure to simulated primary heavy water with a CAMECA IMS7f device. This device is a dynamic SIMS, meaning analysis is performed in the course of abrasion by the primary ion beam. The configuration chosen in the present work allowed depth profiling. A primary Cs^{+} ion beam (40 nA) was used over a 125 x 125 µm² raster surface and the analyzed area was limited to a 33 µm diameter disc in the center of the raster via a system of diaphragms. Several elements were analyzed: ^{1}H, ^{2}H, ^{12}C, ^{16}O, ^{52}Cr, ^{56}Fe, ^{58}Ni. The raw species profiles are expressed in counts per second as function of abrasion time. The abrasion rate depends on the matrix, whereas the ionization rate depends on both the element and the matrix it occupies. To compare the results of the different samples, in order to avoid the influence of small variations of experimental parameters, the signal intensities were systematically normalized to the signal of ^{58}Ni taken deep in the bulk. The ^{2}H signal followed an additional post-treatment, detailed later on in the paper.

After each analysis, the average crater depth was measured with a stylus profiler (Dektak©, Bruker™), addressing an average sputtering rate (associated with this specific run) used to convert the abrasion time (s) into a distance from the surface (nm or µm).

3. RESULTS AND DISCUSSION

3.1. Microstructural characterization

3.1.1. Reference material

The reference material was characterized by optical and electron microscopies. The mean grain size was estimated at 26 ± 6 µm from a polished and electrochemically etched (oxalic acid) sample. The material presented an austenitic structure with around 3% of ferrite islands and scarce Ti(C,N) or oxide precipitates (Figure 3.a). TEM observations revealed the presence of few dislocations (Figure 3.b) : a dislocation density ρ around 10^{13} m^{-2} was estimated by the intercepts method on different areas of the thin foil, where $\rho = n/L^2$ with n the number of dislocations intercepting an line of length L. This value being relatively low, the reference material will thereafter be considered as defectless with respect to dislocations.

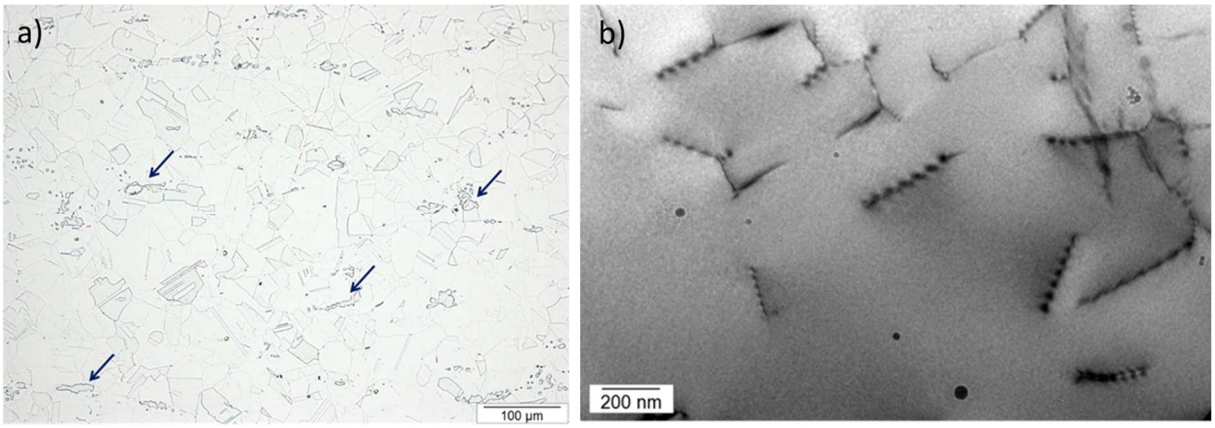

Figure 3 : Microstructure of the reference 316L SS: a) Optical micrograph; The arrows indicate small ferrite islands. b) Bright field TEM micrograph showing dislocations; the thin foil was prepared in the bulk of the specimen.

3.1.2. Fe^{3+} implanted samples

The density and size of implantation-induced defects (Frank loops and cavities) were quantified from TEM observations performed on each type of Fe^{3+} implanted samples (JANNuS#1 and JANNuS#2).

3.1.2.1. Frank dislocation loops distribution

Figure 4 shows a TEM dark-field image of the sub-surface (the surface is highlighted by the dashed line) of the thin foil sampled in JANNuS#2 specimen. It evidences the presence of faulted Frank loops with a wide range of sizes. As these loops were not properly visible in bright field imaging, they were characterized from the dark field images according to the method described in 2.2. The loop density

and size were estimated as a function of their distance from the implanted surface by about 200 nm wide 'slices' parallel to the surface, measured from mosaic of 30 TEM images. Figure 5 illustrates the distribution of these Frank dislocation loops in the two implanted materials. For both specimens, the total average density and mean diameter of dislocation loops measured over the entire implanted zone were estimated around $1.0 \pm 0.1 \times 10^{22}$ m^{-3} and 12.5 nm, respectively. The standard deviation related to the mean size of dislocation loops is 15 nm, showing a high variability of the dislocation loops size. The mean size of Frank loops is similar to the values reported by Chen *et al.* (10-12.5 nm) and Miura *et al.* (9.5 nm), on 316 SS irradiated with 3 MeV Fe at 400 °C and 2.8 MeV Fe at 300 °C, respectively [31,32]. The loop density was between a factor 10 and 100 lower in this study, which could be due to the higher irradiation temperature. For comparison, 10 MeV Fe implantation at 450 °C reported in Gupta *et al.* works [33] leads to an average loops density of 5×10^{21} m^{-3}, closer to the results of the present study.

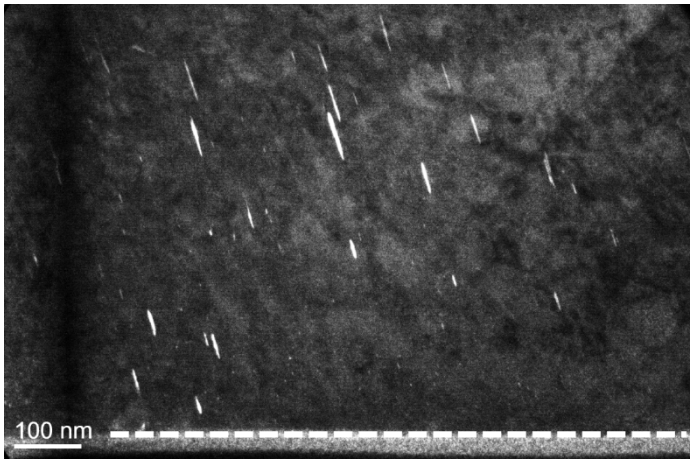

Figure 4 : Dark field TEM micrograph of one family of Frank loops imaged using the rel-rod method. The white dashed line indicates the position of the surface.

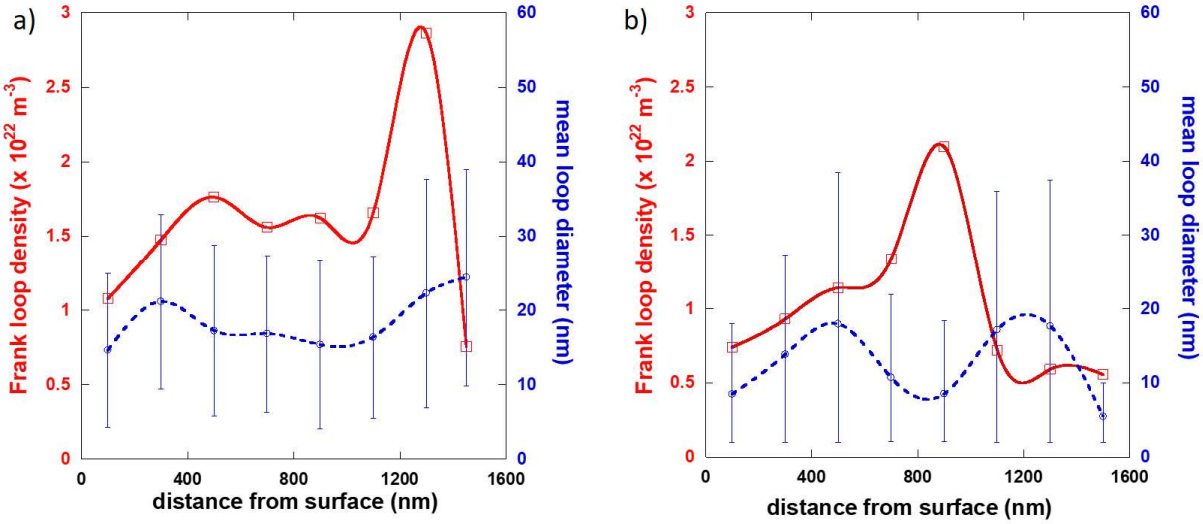

Figure 5 : Frank dislocation loops distribution in JANNuS#1 (a) and in JANNuS#2 (b) specimens, gathering their density (red squares) and mean diameter (blue dashed line). Note that the dispersion in diameter is inherent to the observation method.

The shape of the loop density distribution is in good agreement with the damage distribution given by SRIM simulation for ion implantation even though the highest density of defects is shifted to a somewhat lower depth between 800 and 1000 nm in the case of JANNuS#2 implanted material. An interesting thing to note is the decrease of the loop mean size between 600 and 1000 nm which could be related to the highest density of defects in this zone: dislocation loops are more numerous but smaller.

3.1.2.2. Cavity distribution

Following the same method as for Frank loops, i.e. slice by slice from the surface of the implanted specimen, cavities were characterized by TEM. Figure 6 shows an overfocused TEM micrograph (zoomed in b) taken on the thin foil from JANNuS#2 specimen. Cavity distribution profiles (density and size) as function of the distance from the implanted surface resulting from image analyses are drawn in Figure 7. The two materials JANNuS#1 and #2 differ in these distributions in terms of average size and density. For JANNuS#1, one finds a mean cavity density of $1.7 \pm 0.4 \times 10^{20}$ m^{-3} with a mean diameter of 9 ± 3 nm, whereas for JANNuS#2 the mean cavity density averages $140 \pm 0.3 \times 10^{20}$ m^{-3} with a mean diameter of 5 ± 2 nm, i.e. the cavities are slightly smaller but 100 times more numerous. Refined SIMS profiles at high resolution and slow abrasion rate (primary beam current of 20 nA) carried out on JANNuS#2 specimen (before deuterium charging) evidenced some oxygen accumulation in the implantation-affected zone (not shown): oxygen atoms, co-implanted during JANNuS#2 procedure, could have helped stabilize the cavities. Here again, the maximum defect density was detected at a depth of 800-1000 nm below the surface, differing slightly from what would

be expected according to SRIM calculations (dpa peak at 1200 nm), but which could be consistent with defect recombinations.

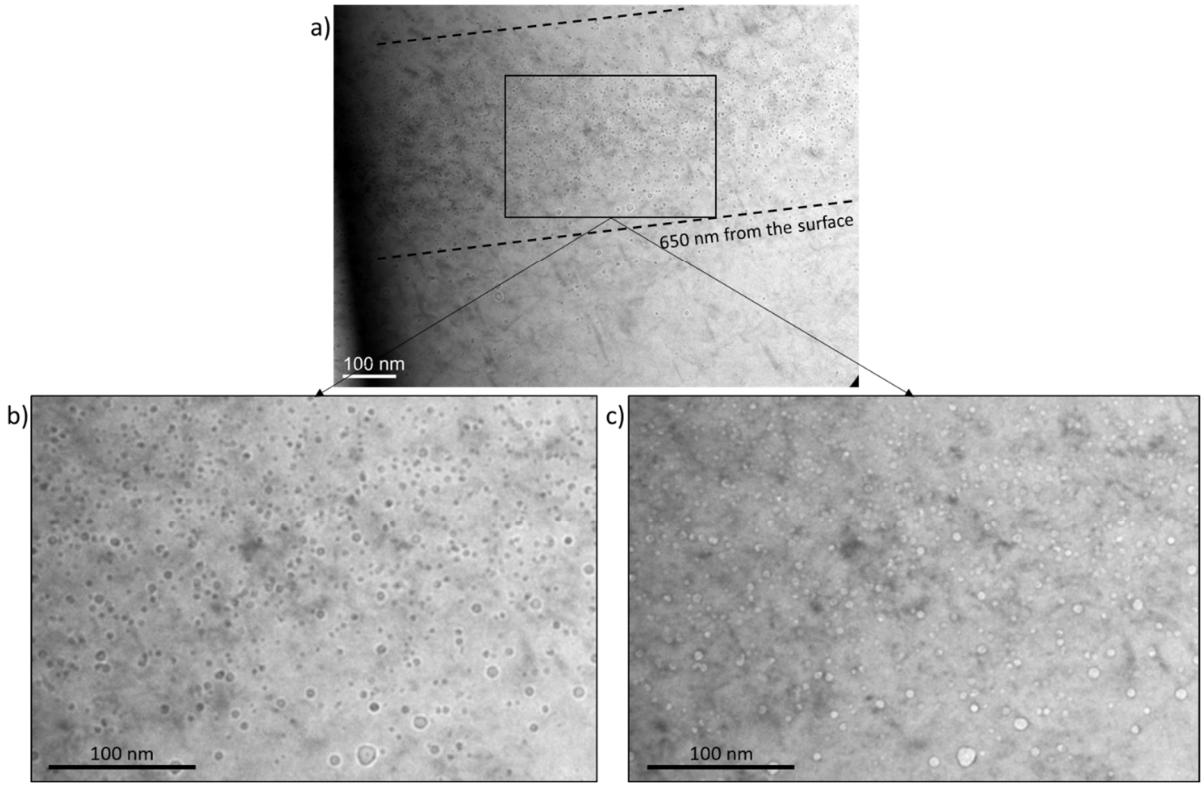

Figure 6 : Bright field TEM micrograph, a) and b) overfocused (+ 1 µm), c) underfocused (- 1 µm), evidencing cavities in JANNuS#2 type specimen. The free surface here is towards the bottom of the images.

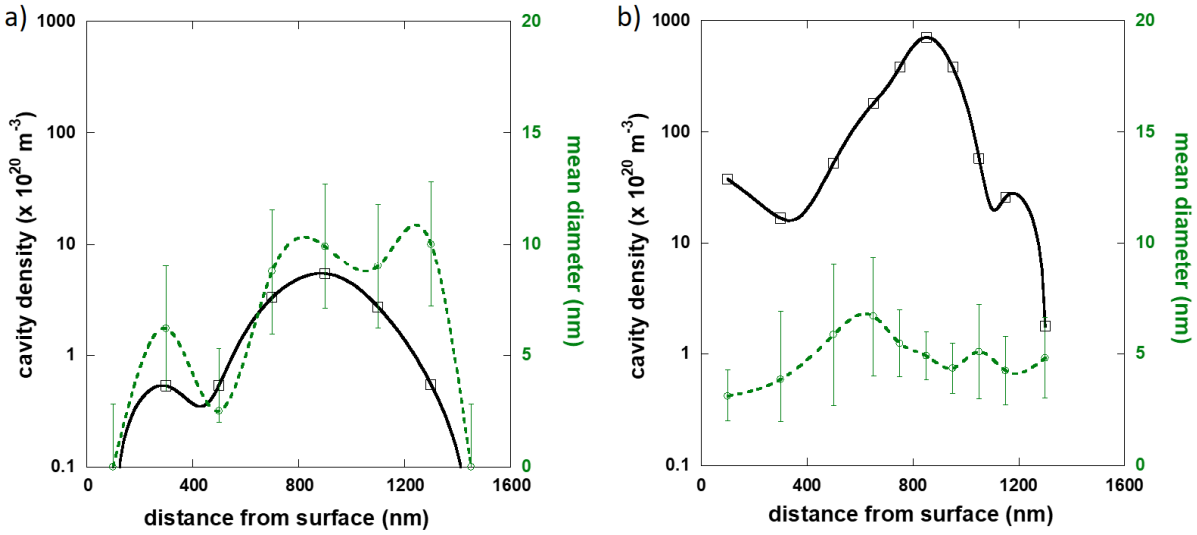

Figure 7 : Cavity density (black line) and mean diameter (green dashed line) distribution from the surface in JANNuS#1 (a) and JANNuS#2 (b) specimens as extracted from TEM analyses. Note that ordinate scale for cavity density is logarithmic and identical in (a) and (b).

3.2. Deuterium distribution in the alloy

The deuterium signals obtained by SIMS depth profiling on the deuterium-charged heat-treated reference sample as well as on both implanted specimens after 24 hours aging at 40 °C under vacuum are presented in Figure 8. The ^{2}H signal of each sample is normalized to the maximum signal of deuterium in the bulk (at around 7 µm) for comparison purpose between specimens and can be assimilated to adimensional concentration profiles.

3.2.1. Heat-treated reference material

The deuterium concentration profile of the heat-treated reference specimen (black curve in Figure 8) decreases strongly from the extreme surface within the first 50-100 nm, probably due to surface contamination or accumulation in the native oxide layer, then rises in a bell shape whose approximate maximum is around 7 µm from the surface. In this material, it is assumed that deuterium atoms occupy only the interstitial sites of the metallic matrix since no trap site is considered. The profile shape results thus from deuterium interstitial diffusion during the aging step, effusing out of the sample by its free surface (the one that was charged) but also deeper in the alloy (flattening and shifting the bell shape distribution towards the bulk). Due to experimental reasons, the full diffusion profile was not recorded, since it would have needed abrasion in the SIMS over tens of hours.

3.2.2. Implanted specimens

In the deuterium SIMS profiles acquired on both deuterium-charged implanted specimens, the overall bell shape of the deuterium distribution in the bulk material is still evidenced, in agreement with the presence, still after the aging time, of deuterium in the interstitial sites of the lattice, which have redistributed during aging by Fick diffusion.

Interestingly the implanted specimen profiles exhibit an additional feature: a clear (for JANNuS#2) – or less obvious (for JANNuS#1) – local accumulation of deuterium is noticed in the 600 – 1200 nm region (from the surface). This feature is in good agreement with the spatial distribution of the implantation-induced defects, for both materials (in the 400 – 1300 nm range as seen earlier). This accumulation is assigned to localized trapping of deuterium in the implantation-affected zone. Hydrogen trapping by implantation-induced defects has indeed already been evidenced by Jambon *et al.* [41] in a nickel-based alloy.

The difference in the deuterium profiles between the two types of specimen may be linked to their different distributions and amounts of defects as characterized in section 3.1.2. Indeed for both JANNuS#1 and JANNuS#2 types, the average Frank loop density and sizes being very similar, deuterium trapping at these defects may not be sufficient to explain the different deuterium concentration profiles observed. The distribution and size of the cavities however vary a lot from a specimen to the other. The JANNuS#2 specimen, that contains more and smaller cavities than JANNuS#1 specimen, presents the most visible accumulation of deuterium. The defects, which contribute more to deuterium trapping, according to these SIMS profiles, would therefore be the cavities. This observation does not discard trapping at dislocation loops or at other potential trap sites such as vacancies ; vacancies are not taken into account in the present study due to lack of experimental evidence on their distribution in the material.

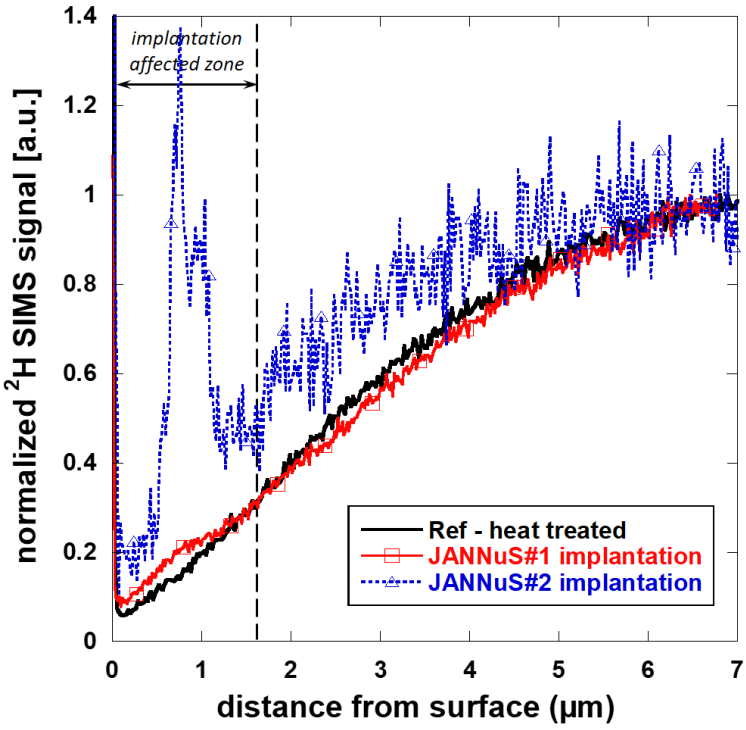

Figure 8 : Normalised deuterium SIMS profiles acquired on implanted – then ^{2}H charged – then aged 24 hours at 40 °C specimens (JANNuS#1 and JANNuS#2). The deuterium profile obtained in the heat-treated reference material is added for comparison.

3.2.3. Specimens exposed to deuterated primary water

In order to analyse the possibility of hydrogen trapping by the irradiation-induced defects during exposure to primary water, the reference material sample as well as both implanted specimens were exposed to simulated primary water, using heavy water as solvent, up to 500 hours. The results will be presented only for the longest duration (500 h). The specimens exposed to simulated primary heavy water were also analysed by SIMS. Before all, the structure of the obtained surface oxide layer must

be recalled. It consists, after 500 h in primary medium, of a duplex oxide layer : a discontinuous outer layer, made of Fe-rich crystallites (spinel structure), covers an inner continuous, Cr-rich layer [15, 42-47], the thickness of the latter ranging around 100 nm [48]. Figure 9 shows the comparison of the SIMS deuterium depth profiles carried out on a reference material and a pre-implanted material (from JANNuS#2 series) after 500 hours exposure in primary media. The normalized signal intensity is in Log scale to enhance details visualization under the oxide layer (otherwise the exacerbation of the signal in the oxide layer completely hinders the details inside the metal). One notices a strong deuterium signal within the first 300 nm, then a decrease in the metallic matrix, and, only for the implanted material, a significant deuterium signal bump around 1000 nm from the surface. This small bump is compared with the one found after cathodic charging of the very same material, showing (different ordinate scale) a strong similarity in shape and depth (black diamonds in Figure 9). At first order, according to the intermediate conclusions mentioned at room temperature for cathodically charged specimens, it evidences trapping of deuterium by irradiation-induced cavities under primary water – type conditions. This suggests three statements: (i) during exposure to primary water, deuterium is incorporated in the bulk material, through the oxide layer, where it can diffuse and interact with defects 'far away' from the oxide/alloy interface; (ii) trapping of deuterium at nanocavities can occur at high temperature (or at least during the cooling down stage) and (ii) deuterium keeps trapped in nanocavities after 500 hours spent in primary water. These statements would nevertheless need further investigations, which will be conducted in the future.

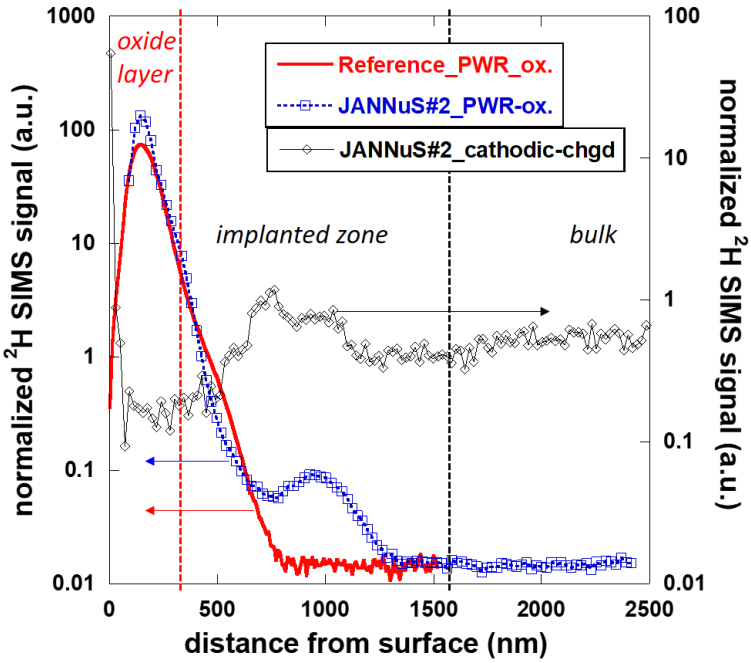

Figure 9 : Normalized (to ^{52}Cr signal in bulk) SIMS ^{2}H profiles on reference (red line) and JANNuS#2 implanted (blue squares) specimens after 500 h oxidation in heavy primary water (11.8 MPa, 320 °C). The ^{2}H SIMS profile obtained after cathodic charging (black diamonds) at room temperature is recalled. Note that here the SIMS signals are represented according to a Log scale.

As mentioned in previous studies [15,49] on 316L SS oxidation in deuterated primary water, the Cr-rich oxide layer contains deuterium, uptaken during the corrosion process. In Figure 9, this corresponds to the deuterium peak within the first 300 nm from the surface. In addition, GD-OES analysis [15] evidenced an accumulation of deuterium (on reference material) in the alloy, just below the oxide / metal interface, not visible in the SIMS depth profile due to interface crossing. One can however assume that beyond 600 nm deep, the SIMS profile can be reliably assigned to the deuterium profile inside the alloy, considering the average thickness of the entire duplex oxide layer ranging around 200 nm [48]. The study of the deuterium accumulation below the oxide/alloy interface and its link with a vacancy density, to be compared with trapping in nanocavities, deserves further investigations. It could imply the coupled use of GD-OES, SIMS and positron annihilation spectroscopy (PAS) for instance.

3.3. Contribution of simulation

As mentioned in section 2.4, simulation was used as an experiment design tool. It was also needed to test the aforementioned hypotheses concerning the main trapping system in implanted materials, i.e. nanocavities versus dislocation loops.

A diffusion and trapping model, detailed elsewhere [39], based on the numerical resolution of the coupled equations of McNabb and Foster [38], was adapted and used to simulate deuterium entry in the stainless steels (cathodic charging step) without and with a specific trap distribution, and its redistribution during aging (adjusted to the experimental conditions). Simulated deuterium concentration profiles were then compared with SIMS analysis deuterium profiles. For the reference material, only pure Fick diffusion was taken into account (absence of traps). The considered equations [38,39] are presented below. Eq. 1 corresponds to the second Fick's law with a trapping term (left part) and Eq. 2 describes the kinetic equation of the deuterium trapping/detrapping.

$$\frac{\partial C_{int}}{\partial t} + N_{Trap}\frac{\partial \theta}{\partial t} = D\frac{\partial^2 C_{int}}{\partial x^2} \quad \text{(Eq.1)}$$

$$\frac{\partial \theta}{\partial t} = k(1-\theta)C_{int} - p\theta \quad \text{(Eq.2)}$$

where C_{int} represents the local interstitial deuterium concentration, N_{Trap} is the trap site density, θ the trap occupancy. D is the interstitial diffusion coefficient of deuterium, k and p the respective trapping and detrapping kinetic constants associated with one type of trap site, all three following an Arrhenius law (Eq. 3 - 5).

$$D = D_0\, exp\left(\frac{-E_D}{RT}\right) \quad \text{(Eq.3)}$$

$$k = k_0 \, exp\left(\frac{-E_k}{RT}\right) \quad \text{(Eq.4)}$$

$$p = p_0 \, exp\left(\frac{-E_p}{RT}\right) \quad \text{(Eq.5)}$$

where D_0 includes the entropic and jump probability terms for diffusion via the lattice interstial sites, E_D corresponds to the migration enthalpy. k_0 and p_0 include the entropic and jump probability terms for trapping and detrapping respectively, and E_k and E_p are the trapping and detrapping activation energies, respectively.

The versatility of the numerical tool used permits to take into account all experimental steps, as well as the initial trap distribution function $N_{Trap}(x)$ in the matrix: the trap density is not uniform in the present case.

In all calculations presented thereafter, the complete charging-aging experimental series applied to the specimens were simulated, following the boundary conditions detailed in Table 2.

Table 2 : List of the boundary conditions corresponding to the experimental history of the specimens used for the simulation of the final deuterium concentration profiles obtained in SIMS.

Initial conditions	
Reference material	***Implanted material***
$\boldsymbol{C_{H,int}\,(t=0,x)=0}$	$C_{H,int}\,(t=0,x)=0$
$\boldsymbol{C_{H,trap}\,(t=0,x)=0}$	$C_{H,trap}\,(t=0,x)=0$
$\boldsymbol{N_{Trap}(t,x)=0}$	$N_{Trap}(t,x)=N_{Trap}(x)$
Charging conditions ***(all materials)***	
$\boldsymbol{C_{H,int}\,(t_1,x=0)=C^0}$ $\boldsymbol{t_1 \in [0;3600]\ s}$ $\boldsymbol{T_1 = 298\ K}$	
Aging conditions ***(all materials)***	
$\boldsymbol{C_{H,int}\,(t_2,x=0)=0}$ $\boldsymbol{t_2 \in [0;86400]\ s}$ $\boldsymbol{T_2 = 313\ K}$	

The nature of the trap distribution function $N_{Trap}(x)$ and its link with the defects distributions in the matrix will be detailed later on.

3.3.1. Determination of the diffusion constants

Since deuterium interstitial diffusion takes place in the reference specimen (“pure” diffusion) and in the implanted specimens (“diffusion + trapping”), the diffusion coefficient needs first to be addressed.

The literature provides self-consistent values for the diffusion coefficient of hydrogen in stainless steels, and more specifically 316L SS, which is extensively documented [40,45-48]. Extrapolation of these data via an Arrhenius-type behavior gives initial values for the pre-exponential constant D_0 and migration enthalpy E_D of the interstitial hydrogen diffusion coefficient : $D_0 = 1 \times 10^{-3}$ cm².s^{-1} and E_D = 45 kJ.mol^{-1} [40]. These values were used as a starting point and adjusted so that simulations of concentration profiles fit at best the experimental SIMS profiles. This procedure has the advantage to take into account any defect-affected diffusion in the heat-treated reference material, as well as possible short-circuit diffusion via grain boundaries, and dissociate it from any additional trapping contribution to the deuterium transport.

Depth profile fitting to adjust these parameters was performed using the deuterium SIMS profile obtained on the heat-treated reference specimen. After adjustment, a matching pair of values was found:
$D_0 = 1.4 \times 10^{-5}$ cm².s^{-1} and $E_a = 40$ kJ.mol^{-1}. The comparison between experimental data and simulation with this set of diffusion coefficient constants is shown in Figure 10.

The values determined here for deuterium diffusion in interstitial sites in 316L stainless steel are fairly in good agreement with literature data [40,50-54] but show some discrepancies, especially on the value of the diffusion coefficient at room temperature (5 to 10 times lower in the case of the present study). The origin of this difference could be that other matching pairs of values would adjust our SIMS experimental data. However, since all three materials followed the same thermal history, from elaboration to deuterium charging and aging, the as-found pair of values was assumed sufficiently reliable to be directly injected in the numerical model for the simulation of diffusion and trapping of deuterium in the implanted 316L stainless steels.

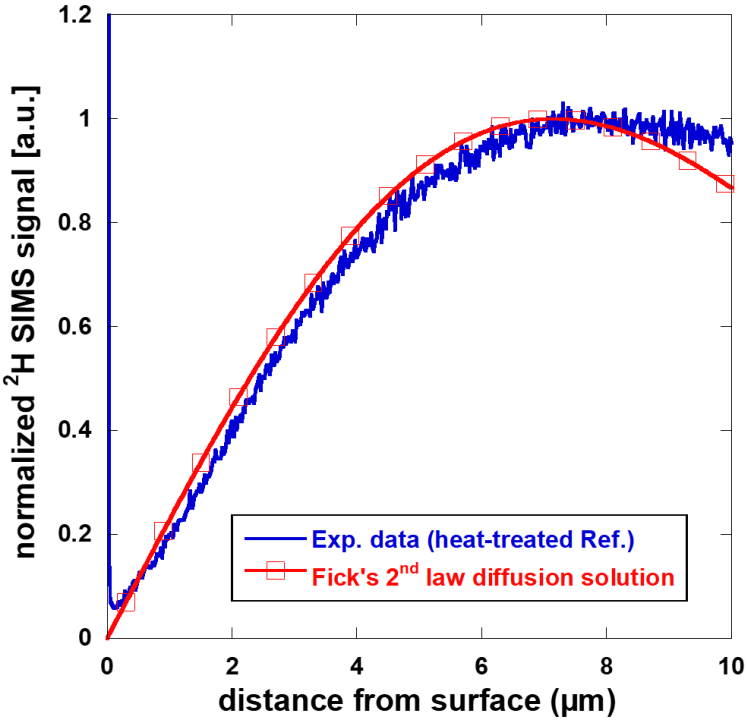

Figure 10 : Comparison between the simulated depth profile (using Fick's second law and taking into account the history of charging and aging) with the experimental deuterium profile obtained on the heat-treated reference specimen. Simulation was performed with optimized D_0 and E_D values.

3.3.2. Trapping of deuterium in the implanted materials

At its development state, the numerical model only considers one type of trap site. The way to deal with two potential trap sites, like in the present case dislocation loops and cavities, is to consider them separately, assuming that one type of defects accounts for the majority of trapped deuterium. First, Frank dislocation loops were considered as main trap sites for deuterium, then cavities.

3.3.2.1. Frank dislocation loops

The values of the parameters k_0, E_k, p_0 and E_p for Frank dislocation loops do not exist in the literature. However, they are available for edge dislocations in a nickel-based alloy, based on recent works by Hurley [40]. These values will be assumed, at first order, usable for trapping at Frank dislocation loops in austenitic stainless steels, and are gathered in Table 3. The other essential input parameter for the code is the trap sites density $N_{Trap}(t,x)$, which in the present case depends on the distance from the surface x and has to be linked to the defect density. It was assumed that this trap distribution did not evolve with time: $N_{Trap}(t,x) = N_{Trap}(x)$. In former works, Hurley [40] and Chêne *et al.* [55] attempted to estimate proportionality relationship between the dislocation density and the hydrogen trap site density

associated with edge dislocations. Typical values range between 10 and 50 hydrogen atoms that can be trapped per Burger's vector of edge dislocations. For practical reasons, it was assumed that a dislocation loop of perimeter *l* was equivalent to a dislocation of length *l*. The Frank dislocation loops distributions (density and size), presented in section 3.1.2, were converted into an equivalent linear dislocation density as function of depth, as shown in Figure 11.a. This dislocation density distribution has in turn been converted into a trap sites distribution in the implanted specimens thanks to a proportionality factor α (ranging between 10 and 50) linking trap and dislocation densities. In the present case, α has been taken equal to 12 as in [40].

Table 3 : Trapping (k) and detrapping (p) kinetic constants for trapping at dislocations in A600 nickel-based alloy [40]; these values were used in the present study for the 316L austenitic stainless steel.

trapping at dislocations (*k*)		**detrapping from dislocations (*p*)**	
k_0 ($cm^3.mol^{-1}.s^{-1}$)	E_k ($kJ.mol^{-1}$)	p_0 (s^{-1})	E_p ($kJ.mol^{-1}$)
$(1.5 \pm 0.2)\ 10^6$	42 ± 4	$(1.5 \pm 0.2)\ 10^6$	76 ± 4

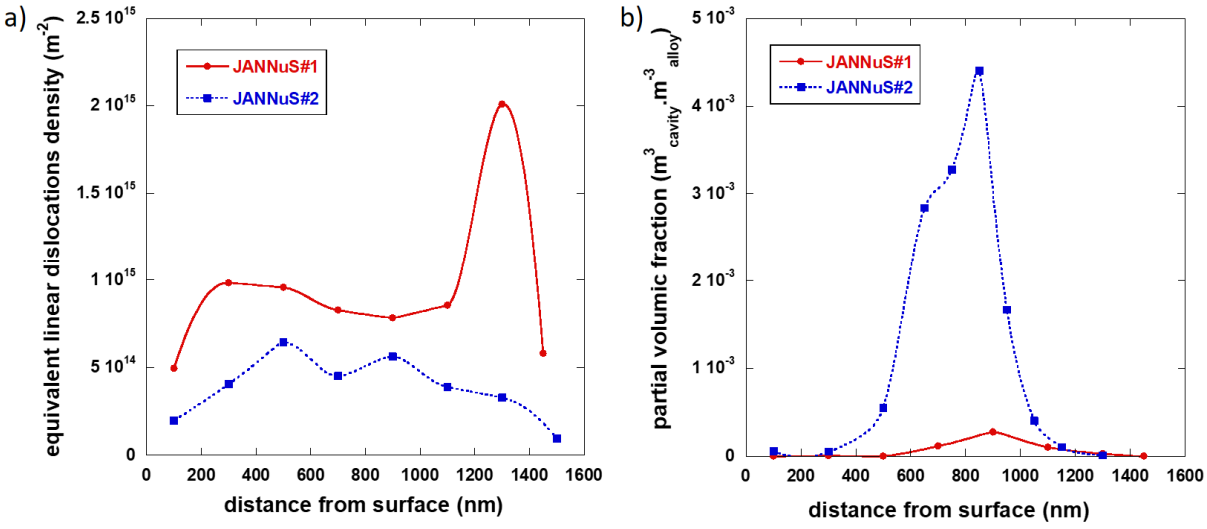

Figure 11 : Effective implantation defects distribution profiles obtained from TEM measurements, after transformation a) of Frank loop density and size into an equivalent linear dislocation density, and b) of cavity density and size into a partial volume fraction of cavities. Both implantation sets defects profiles are represented: JANNuS#1 in red circles, JANNuS#2 in blue squares.

The result of the simulation of the deuterium depth profile for JANNuS#2 specimen after cathodic charging (3 h at 25 °C) and aging for 24 h at 40 °C with these parameters is presented in Figure 12.a, along with the normalized SIMS experimental deuterium profile. The experimental concentration

profile is on average well-reproduced by the simulation using this preliminary set of parameters. Beyond 3 µm from the surface, the two profiles are well-superimposed indicating a good reproduction by simulation of the interstitial deuterium profile, validating the hypothesis made on the invariance of diffusion coefficient. The zone where deuterium is trapped by implantation-induced defects is broader with simulation than in reality. With the current data, the trapping and detrapping kinetic parameters, k and p, extracted from literature [40], seem however to be applicable to dislocation loops. The conversion factor α value of 12 seems also relevant. The very same methodology was applied to JANNuS#1 type deuterium profile, with injection of the equivalent trap site density associated with its Frank dislocation loops distribution and the same α factor value. Figure 12.b shows the comparison between simulated concentration profile and normalized SIMS profile. Again, the interstitial deuterium contributions are in good agreement. However, a large discrepancy between simulation and experiments is observed in the implantation-affected area. The simulation forecasts a much higher deuterium accumulation than that observed experimentally. This result is not surprising, since both types of specimens have been shown to contain similar dislocation loop density and sizes, whereas experimental SIMS profiles differed a lot in terms of relative intensity in this zone. It nonetheless confirms that trapping at Frank dislocation loops may not be the main contribution to local deuterium accumulation experimentally observed in the implantation-affected zone.

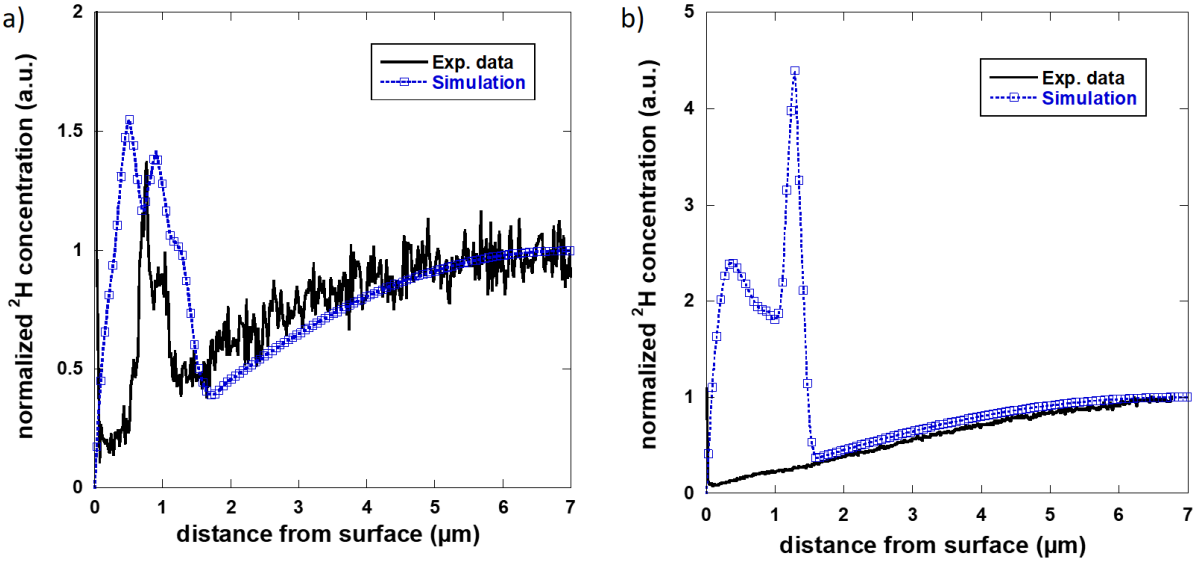

Figure 12 : Direct comparison of normalized deuterium concentration profiles obtained by SIMS (black curve) and by simulations (blue squares) taking into account Frank dislocations loops only as trap sites for hydrogen: a) JANNuS#2 and b) JANNuS#1 implantation sets.

3.3.2.2. Cavities

A similar methodology was applied for cavities. However, in this case, no data concerning trapping or detrapping kinetics was found in literature, nor any attempt to link cavity size to any hydrogen trap site

density. It is generally admitted that cavities, or internal cracks, would form traps with high binding energies (i.e. high detrapping activation energy E_p) [56,57], higher than for dislocations, and that they form unsaturable trap sites (since some internal recombination of hydrogen atoms into molecular hydrogen can occur [58]). Nonetheless, the use of the trapping/detrapping kinetic constants associated with dislocations is acceptable, keeping in mind it consists in a minoring effect of trapping. Associated constants will be addressed in future works. The question of the link between the cavity distribution in size and density and the trap site density was addressed as follows: the trap site density $N_{Trap}(x)$ was assumed as the product between the volume fraction of cavities (shown in Figure 11.b) and a factor β corresponding to the number of trap site per cavity volume unit (in m^{-3}). Note that a surface density could also have been used, resulting in similar conclusions. This factor β was manually adjusted so that the simulated concentration profile 'peak intensity' fits to the experimental one, meanwhile keeping the balance with interstitial deuterium (maximum of the bell-shaped profile at around 7 µm from the surface). The β factor value adjustment was performed only on JANNuS#2 data, then set for JANNuS#1 SIMS profile simulation. A good estimate for β was found as 4×10^{27} traps.m^{-3}_{cavity}.

Comparison of simulated concentration profiles with experimental SIMS data (Figure 13) shows a very good agreement for both types of specimens.Figure 13.a shows a very faithful reproduction of the experimental concentration profile obtained on JANNuS#2 specimen, with a better accuracy than when considering dislocation loops in terms of spatial distribution. For JANNuS#1 specimen, even the small bump in the implantation-affected zone is reproduced, with a correct balance between interstitial hydrogen and trapped hydrogen (see Figure 13.b). Some slight discrepancies between simulation and experimental data still remain, and the code would certainly need refining, but considering all the first order assumptions made, it shows it is capable of relatively good accuracy and permits to render experimental distributions of deuterium in the material, provided the defect distribution is well characterized and that the main trap site is identified.

A piece of the JANNuS#2 specimen, cathodically deuterium-charged in identical conditions, was submitted to thermal desorption. The set-up used is home-made (see more details in [39,40]) and uses a quadrupole mass spectrometer to detect and record the deuterium desorption flux. The ionic current is calibrated thanks to standard deuterium gas leaks in order to convert it into a $mol_D.s^{-1}$ flux. A 10 $K.min^{-1}$ temperature ramp was applied to the specimen up to 1050 °C so that all deuterium in the specimen was outgassed and measured. Based on the integration of the TDS signal over time, the amount of deuterium inside the specimen just after charging was quantified, allowing the estimation of the surface concentration C^0, which was then used in calculations to quantify the deuterium profile in the material. The same procedure was applied to JANNuS#1 specimen. Figure 14 gathers the quantified trapped deuterium profiles associated with trapping by nanovoids for both types of specimens. One reaches local concentrations of deuterium as high as 86 at.ppm in the case of

JANNuS#2, whereas only about 5 at.ppm are highlighted in JANNuS#1 specimen, in agreement with the normalized profiles (Figure 13).

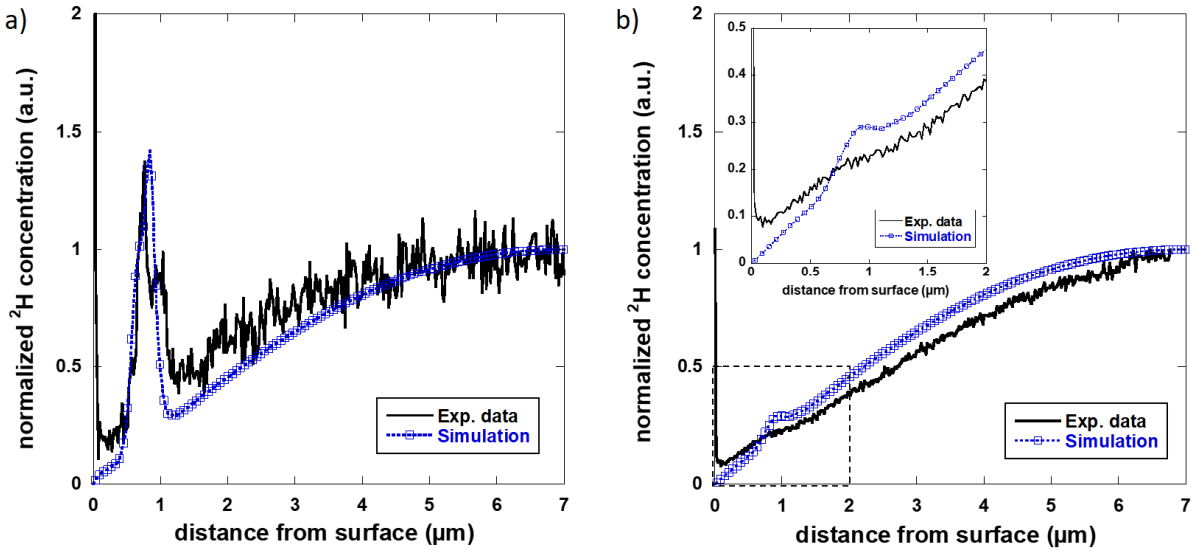

Figure 13 : Direct comparison of normalized deuterium concentration profiles obtained by SIMS (black curve) and by simulations (blue squares) taking into account the cavities only as trap sites for hydrogen: a) JANNuS#2 and b) JANNuS#1 implantation sets. Insert in b) zooms in the 0-2 µm area from surface.

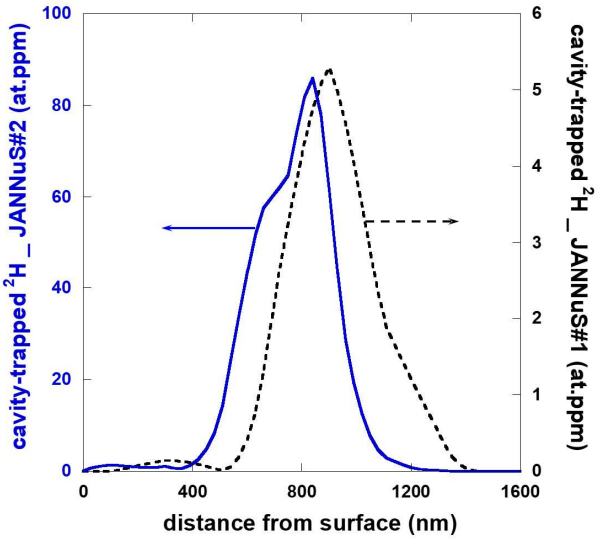

Figure 14 : Quantified deuterium distribution at voids for JANNuS#1 specimen (right, black dotted line) and for JANNuS#2 specimen (left, blue line) within the first 1600 nm from the surface.

The number of deuterium atoms per cavity could be eventually estimated. The average void density, for instance in JANNuS#2 specimen, over the most-affected depth layer of the specimen (i.e. between

400 and 1100 nm depth according to Fig.11) was estimated at 2.62 x 10^{22} m^{-3}, with an average void diameter of 5.5 nm. In the same representative volume, integration of the curve presented in Figure 14 gives an average trapped deuterium concentration of 40 at.ppm. This leads to an average of 130 of ^2H atoms per void. The identification of the state of these deuterium atoms inside the voids (ad atoms on the void surface or recombined as $^2H_2$ molecules) is however unclear at this stage of our investigations.

Further works are needed to better understand the detrapping mechanisms of hydrogen species at cavities, as well as their associated kinetic constants. In order to be more relevant to in-core irradiation and hydrogen trapping mechanisms occurring during the corrosion process in primary water, the next step would be to implement the code to : (i) model trapping under primary water conditions in terms of temperature and hydrogen uptake kinetics, and (ii) take into account the evolution of the defects with time under continuous irradiation and hydrogen uptake.

In the present study, we chose to perform ion implantation and hydrogen cathodic charging separately and assumed in the modelling that hydrogen introduced in the alloy did not modify the defects population characterized after ion implantation. Nevertheless, in PWR primary medium, hydrogen uptake occurs simultaneously with neutron irradiation and the interaction between this element and irradiation defects could modify the final alloy damaged microstructure. For example, Kato *et al.* [59] studied the interactions between hydrogen and implantation-induced defects by H^+ and H_2^+ implantations in various annealed stainless steels. They showed that hydrogen modifies the cavity population and allows cavities to form at the grain boundaries. Thus, another way to improve the modelling will be to consider the hydrogen effects on implantation-induced defects and it will start by TEM characterizations of defects in an implanted sample after hydrogen charging, in order to adjust trapping site density and location in the simulation.

4. CONCLUSIONS

In this work, to study the interactions between hydrogen and irradiation-induced defects, an annealed 316L stainless steel was implanted with 5 MeV Fe^{3+} ions at 500 °C in order to simulate defects created by neutron irradiation. The implanted microstructure was thoroughly characterized by TEM, which led to the identification of implantation defects (Frank loops and nanocavities or voids) and their distribution from the surface. Deuterium cathodic charging, as well as exposure to simulated primary heavy water, combined with SIMS analyses allowed focusing on hydrogen species interactions with these implantation-induced defects.

Original numerical calculations, involving for the first time the input of a depth-dependent trap density, were performed. Their specificity rely on the direct injection as input data of the

experimentally-determined Frank loops or voids density distributions as equivalent trap site density distributions, used to simulate diffusion and trapping of hydrogen in the implanted materials. A very good agreement was achieved between the experimental and the simulated data.

The main results of present works can be summarized as follows:

- 316L SS irradiation under 5 MeV Fe^{3+} ions at 500 °C generated Frank dislocation loops and voids, whose distribution in volume (within the two first micrometers from the surface) were fully characterized by TEM;
- Deuterium cathodic charging and SIMS depth profiles permitted to evidence deuterium accumulation in the implantation-affected zone;
- Such accumulation was evidenced to be efficient also at high temperature (tests carried out in simulated deuterated primary water at 320 °C) at the vicinity of the implantation-affected zone, suggesting hydrogen trapping can occur during corrosion in NPP core.
- An original numerical simulation method, injecting all experimental parameters and depth-dependent defect distribution as trap sites for deuterium, allowed assigning such accumulation of hydrogen (deuterium) to trapping at voids.
- About 130 deuterium atoms were trapped per void on average.

This work opens the way to the use of numerical calculations to estimate, from irradiation-induced defect profiles or distribution in 316L SS, the associated hydrogen distribution encountered under corrosion conditions in primary water, knowing their time or temperature evolution. Such information may serve as input data for SCC or IASCC structural evolution (or mechanics) numerical codes, taking into consideration the local hydrogen content. Nevertheless, further experiments and simulations are needed to carefully characterize the trapping/detrapping parameters of hydrogen/deuterium at voids. The distribution of vacancies, not accessible by TEM, will also be the subject of future works. Finally, future works will be dedicated to the acquisition of data allowing the simulation of a dynamic system accounting for continuous *in situ* hydrogen uptake and irradiation, more representative of the in-core situation.

ACKNOWLEDGMENTS

The authors would like to thank Y. Serruys, E. Bordas and Team JANNuS (DMN/JANNUS, CEA Saclay) for their support and assistance in conducting the Fe irradiations. The authors would also like to acknowledge K. Rousseau (SERMA TECHNOLOGIES, Grenoble, France) for preparing and providing the FIB TEM thin foils.

REFERENCES

[1] P. Scott, “A review of irradiation assisted stress corrosion cracking,” *J. Nucl. Mater*. 211 (1994) pp. 101–122.

[2] G. S. Was, Y. Ashida, and P. L. Andresen, “Irradiation-assisted stress corrosion cracking,” *Corros. Rev*. 29 (2011) pp. 7–49.

[3] G. Pressouyre, “Trap theory of hydrogen embrittlement”, *Acta Metall*. 28 (1980) pp. 895–911.

[4] A.-M. Brass and J. Chêne, “Hydrogen uptake in 316L stainless steel: Consequences on the tensile properties”, *Corros. Sci*. 48 (2006) pp. 3222–3242.

[5] I. M. Robertson, P. Sofronis, A. Nagao, M. L. Martin, S. Wang, D. W. Gross, K. E. Nygren, “Hydrogen Embrittlement Understood”, *Metall. Mater. Trans. B*. 46 (2015) pp. 1085–1103.

[6] J. Chêne and F. Martin, “Isotopic tracing of hydrogen transport and trapping in nuclear materials”, *Phil. Trans. R. Soc. A* 375 (2017) p. 20160406.

[7] C. Beachem, “A new model for hydrogen-assisted cracking”, *Metall. Trans*. 3 (1972) p. 441-455.

[8] S.P. Lynch, “Environmentally assisted cracking: overview of evidence for an adsorption-induced localised-slip process”, *Acta Metall*. 36 (1988) pp. 2639–2661.

[9] V. G. Gavriljuk, V. N. Shivanyuk, J. Foct, “Mechanisms of Hydrogen Embrittlement of Austenitic Stainless Steels”, *J. Mech. Behav. Mater*. 16 (2005) pp. 163-175.

[10] H. K. Birnbaum and P. Sofronis, “Hydrogen-enhanced localized plasticity—a mechanism for hydrogen-related fracture”, *Mater. Sci. Eng. A* 176 (1994) pp. 191-202.

[11] L. Marchetti, F. Martin, F. Datcharry, J. Chêne, “Kinetics of hydrogen permeation through a Ni-base alloy membrane exposed to primary medium of pressurized water reactors”, *Corros. Sci*. 144 (2018) pp. 1-12.

[12] N. Totsuka and Z. Szklarska-Smialowska, “Effect of electrode potential on the hydrogen-induced IGSCC of alloy 600 in an aqueous solution at 350°C”, *Corrosion* 43 (1987) pp. 734–738.

[13] R. Rios, T. Magnin, D. Noel, O. de Bouvier, “Critical analysis of alloy 600 stress corrosion cracking mechanisms in primary water” *Metall. Mater. Trans. A* 26 (1995) pp. 925–939.

[14] X. Zhong, S. C. Bali, T. Shoji, “Effects of dissolved hydrogen and surface condition on the intergranular stress corrosion cracking initiation and short crack growth behavior of non-sensitized 316 stainless steel in simulated {PWR} primary water”, *Corros. Sci*. 118 (2017) pp. 143–157.

[15] M. Dumerval, S. Perrin, L. Marchetti, M. Tabarant, F. Jomard, Y. Wouters, "Hydrogen absorption associated with the corrosion mechanism of 316L stainless steels in primary medium of Pressurized Water Reactor (PWR)", *Corros. Sci*. 85 (2014) pp. 251–257.

[16] N. Hashimoto, E. Wakai, J. P. Robertson, "Damage structure in austenitic stainless steel 316LN irradiated at low temperature in the HFIR", *J. Electron Microsc*. 48 (1999) p. 575-580.

[17] D. J. Edwards, E. P. Simonen, S. M. Bruemmer, "Evolution of fine-scale defects in stainless steels neutron-irradiated at 275 °C", *J. Nucl. Mater*. 317 (2003) pp. 13–31.

[18] G. S. Was and P. L. Andresen, "Stress corrosion cracking behavior of alloys in aggressive nuclear reactor core environments", *Corrosion* 63 (2007) pp. 19–45.

[19] O. K. Chopra and A. S. Rao, "A review of irradiation effects on LWR core internal materials - IASCC susceptibility and crack growth rates of austenitic stainless steels", *J. Nucl. Mater*. 409 (2011) pp. 235–256.

[20] Y. Dong, B. H. Sencer, F. A. Garner, and E. A. Marquis, "Microchemical and microstructural evolution of AISI 304 stainless steel irradiated in EBR-II at PWR-relevant dpa rates", *J. Nucl. Mater.* 467 (2015) pp. 692–702.

[21] Q. Xu and J. Zhang, "Effects of He, D interaction on thermal desorption of He and D2 and microstructural evolution in pure Fe", *J. Nucl. Mater.* 479 (2016) pp. 255-259

[22] S.A. Karpov, I.E. Kopanets, B.S. Sungurov, G.D. Tolstolutskaya, A.S. Kalchenko, "Microstructure evolution and deuterium retention in SS 316L steel irradiated with heavy ions, helium and hydrogen", *East Eur. J. Phys.* 2 (2015) pp. 72-79

[23] S.A. Karpov, G.D. Tolstolutskaya, B.S. Sungurov, V.V. Ruzhytskiy, "Microstructure evolution and deuterium trapping in low-energy cascades after irradiation of SS 316L stainless steel", ISSN 1562-6016. *PAST*. 2017 2 (108), pp. 36-40.

[24] V.N. Voyevodin, S.A. Karpov, I.E. Kopanets, V.V. Ruzhytskyi, G.D. Tolstolutskaya, F.A. Garner, "Influence of displacement damage on deuterium and helium retention in austenitic and ferritic-martensitic alloys considered for ADS service", *J. Nucl. Mater*. 468 (2016) pp. 274-280

[25] I. P. Chernov, Yu. P. Cherdantsev, A. M. Liber, G. V. Garanin, A. S. Surkov, "Behavior of hydrogen in stainless steel under irradiation", *J. Surface Investigation. X-ray, Synchrotron and Neutron Techniques* 1 (2007) pp. 373–379

[26] F.A. Garner, E.P. Simonen, B.M. Oliver, L.R. Greenwood, M.L. Grossbeck, W.G. Wolfer, P.M. Scott, "Retention of hydrogen in fcc metals irradiated at temperatures leading to high densities of bubbles or voids", *J. Nucl. Mater*. 356 (2006) pp. 122-135

[27] G. S. Was, J. T. Busby, T. Allen, E. A. Kenik, A. Jenssen, S. M. Bruemmer, J. Gan, A. D. Edwards, P. M. Scott and P. L. Andreson, "Emulation of neutron irradiation effects with protons: validation of principle," *J. Nucl. Mater*. 300 (2002) pp. 198–216.

[28] G. S. Was, Fundamentals of Radiation Materials Science: Metals and Alloys. Springer Science & Business Media, 2007.

[29] C. Xu, G. Zhang, W. Qian, J. Mei, X. Liu, C. Li, F. Xue, J. Li, H. Liu, "Positron annihilation lifetime studies of stainless steel under proton and Xe irradiation", *Fusion Engineering and Design* 120 (2017) pp. 34–38

[30] J. Gan and G. S. Was, "Microstructure evolution in austenitic Fe–Cr–Ni alloys irradiated with protons: comparison with neutron-irradiated microstructures", *J. Nucl. Mater.* 297 (2001) pp. 161–175.

[31] D. Chen, K. Murakami, K. Dohi, K. Nishida, N. Soneda, Z. Li, L. Liu, N. Sekimura, "Depth distribution of Frank loop defects formed in ion-irradiated stainless steel and its dependence on Si addition", *Nucl. Instrum. Methods Phys. Res. Sect. B Beam Interact. Mater. At*. 365 (2015) pp. 503–508.

[32] T. Miura, K. Fujii, H. Nishioka, K. Fukuya, "Effects of hydrogen on interaction between dislocations and radiation-induced defects in austenitic stainless steels" *J. Nucl. Mater*. 442 (2013) pp. S735–S739.

[33] J. Gupta, J. Hure, B. Tanguy, L. Laffont, M.-C. Lafont, E. Andrieu, "Evaluation of stress corrosion cracking of irradiated 304L stainless steel in {PWR} environment using heavy ion irradiation", *J. Nucl. Mater*. 476 (2016) pp. 82–92.

[34] Z. Jiao and G. S. Was, "Precipitate behavior in self-ion irradiated stainless steels at high doses", *J. Nucl. Mater.* 449 (2014) pp. 200-206.

[35] A. Etienne, M. Hernandez-Mayoral, C. Genevois, B. Radiguet, P. Pareige, "Dislocation loop evolution under ion irradiation in austenitic stainless steels", *J. Nucl. Mater.* 400 (2010) pp. 56-63.

[36] J. Gupta, "Intergranular stress corrosion cracking of ion irradiated 304L stainless steel in PWR environment", PhD Thesis, Université de Toulouse, 2016.

[37] R. E. Stoller, M. B. Toloczko, G. S. Was, A. G. Certain, S. Dwaraknath, and F. A. Garner, "On the use of SRIM for computing radiation damage exposure", *Nucl. Instrum. Methods Phys. Res. Sect. B Beam Interact. Mater. At*. 310 (2013) pp. 75–80.

[38] A. McNabb and P. K. Foster, “A new analysis of the diffusion of hydrogen in iron and ferritic steels”, *Trans. Metall. Soc. AIME* 227 (1963) pp. 618–627.

[39] C. Hurley, F. Martin, L. Marchetti, J. Chêne, C. Blanc, and E. Andrieu, “Numerical modeling of thermal desorption mass spectroscopy (TDS) for the study of hydrogen diffusion and trapping interactions in metals”, *Int. J. Hydrog. Energy* 40 (2015) pp. 3402–3414.

[40] C. Hurley, “Kinetic study of hydrogen-material interactions in nickel base alloy 600 and stainless steel 316L through coupled experimental and numerical analysis”, Ph-D thesis, Institut National Polytechnique de Toulouse, 2015.

[41] F. Jambon, L. Marchetti, M. Sennour, F. Jomard, and J. Chêne, “SIMS and TEM investigation of hydrogen trapping on implantation defects in a nickel-based superalloy”, *J. Nucl. Mater.* 466 (2015) pp. 120–133.

[42] D. Lister, R. Davidson, E. McAlpine, “The mechanism and kinetics of corrosion product release from stainless-steel in lithiated high-temperature water”, *Corros. Sci.* 27 (1987) pp. 113-140.

[43] B. Stellwag, “The mechanism of oxide film formation on austenitic stainless steels in high temperature water”, *Corros. Sci.*, 40 (1998) pp. 337-370.

[44] T. Terachi, K. Fujii, K. Arioka, “Microstructural Characterization of SCC Crack Tip and Oxide Film for SUS 316 Stainless Steel in Simulated PWR Primary Water at 320°C », *J. Nucl. Sci. Technol.* 42 (2005) pp. 225-232.

[45] R. Soulas, M. Cheynet, E. Rauch, T. Neisius, L. Legras, C. Domain, Y. Brechet, “TEM investigations of the oxide layers formed on a 316L alloy in simulated PWR environment », *J. Mater. Sci.* 48 (2013) pp. 2861-2871.

[46] S. Perrin, L. Marchetti, C. Duhamel, M. Sennour, F. Jomard, “Influence of Irradiation on the Oxide Film Formed on 316 L Stainless Steel in PWR Primary Water”, *Oxid. Met.* 80 (2013) pp. 623-633.

[47] G. Han, Z. Lu, X. Ru, J. Chen, Q. Xiao, Y. Tian, “Improving the oxidation resistance of 316L stainless steel in simulated pressurized water reactor primary water by electropolishing treatment”, *J. Nucl. Mater.* 467 (2015) pp. 194-204.

[48] A.-C. Bach, “Etude du piégeage de l’hydrogène dans un acier inoxydable austénitique dans le cadre de la corrosion sous contrainte assistée par l’irradiation”, PhD thesis, Mines Paristech, PSL Research University, 2018

[49] M. Dumerval, S. Perrin, L. Marchetti, M. Sennour, F. Jomard, S. Vaubaillon, Y. Wouters, “Effect of implantation defects on the corrosion of 316L stainless steels in primary medium of pressurized water reactors”, *Corros. Sci.* 107, Supplement C (2016) pp. 1-8.

[50] W. A. Swansiger and R. Bastasz, “Tritium and deuterium permeation in stainless steels: influence of thin oxide films”, *J. Nucl. Mater*. 85 (1979) pp. 335–339.

[51] P. Tison, “Influence de l’hydrogène sur le comportement des métaux”, Ph-D thesis, Université Pierre et Marie Curie Paris 6, 1984.

[52] C. Shan, A. Wu, Q. Chen, “The behavior of diffusion and permeation of tritium through 316L stainless steel”, *J. Nucl. Mater.* 179 (1991) pp. 322–324.

[53] K. S. Forcey, D. K. Ross, J. C. B. Simpson, D. S. Evans, “Hydrogen transport and solubility in 316L and 1.4914 steels for fusion reactor applications”, *J. Nucl. Mater*. 160 (1988) pp. 117–124.

[54] D. M. Grant, D. L. Cummings, D. A. Blackburn, “Hydrogen in 316 steel — diffusion, permeation and surface reaction”, *J. Nucl. Mater*. 152 (1988) pp. 139–145.

[55] J. Chêne and A. M. Brass, “Hydrogen transport by mobile dislocations in nickel base superalloy single crystals”, *Scripta Mater*. 40 (1999) pp. 537–542.

[56] J.B. Condon and T. Schober, “Hydrogen bubbles in metals”, *J. Nucl. Mater.* 207 (1993) pp. 1-24.

[57] T. Ahlgren, K. Heinola, K. Vörtler, J.Keinonen, “Simulation of irradiation induced deuterium trapping in tungsten”, *J. Nucl. Mater*. 427 (2012) pp. 152-161.

[58] E. Hayward, R. Hayward, C.-C. Fu, “Predicting distinct regimes of hydrogen behavior at nano-cavities in metals”, *J. Nucl. Mater*. 476 (2016) pp. 36-44.

[59]T. Kato, K. Nakata, J. Kuniya, S. Ohnuki, H. Takahashi, “Cavity formation by hydrogen injection in electron-irradiated austenitic stainless steel”, *J. Nucl. Mater*. 155–157 (1988) pp. 856–860.

Figure Captions

Figure 1 : SRIM cumulated mean damage (dpa) simulation for JANNuS#1 (red circles) and JANNuS#2 (blue squares) implantation conditions. The error bars show scattering due to flux measures uncertainties.

Figure 2 : Illustration of the preliminary calculations performed to optimize the charging – aging parameters necessary for enhanced detection of hydrogen atoms trapped by defects in the implanted zone (simulated by the input sigmoid function shown in the insert in a)). The total hydrogen (black curve), the interstitial hydrogen (red squares) and trapped hydrogen (blue diamonds) concentration profiles are represented a) just after charging for 3 hours at 25 °C, and b) after additional aging for 24 hours at 40 °C.

Figure 3 : Microstructure of the reference 316L SS: a) Optical micrograph; The arrows indicate small ferrite islands. b) Bright field TEM micrograph showing dislocations; the thin foil was prepared in the bulk of the specimen.

Figure 4 : Dark field TEM micrograph of one family of Frank loops imaged using the rel-rod method. The white dashed line indicates the position of the surface.

Figure 5 : Frank dislocation loops distribution in JANNuS#1 (a) and in JANNuS#2 (b) specimens, gathering their density (red squares) and mean diameter (blue dashed line). Note that the dispersion in diameter is inherent to the observation method.

Figure 6 : Bright field TEM micrograph, a) and b) overfocused (+ 1 µm), c) underfocused (- 1 µm), evidencing cavities in JANNuS#2 type specimen. The free surface here is towards the bottom of the images.

Figure 7 : Cavity density (black line) and mean diameter (green dashed line) distribution from the surface in JANNuS#1 (a) and JANNuS#2 (b) specimens as extracted from TEM analyses. Note that ordinate scale for cavity density is logarithmic and identical in (a) and (b).

Figure 8 : Normalised deuterium SIMS profiles acquired on implanted – then ^{2H} charged – then aged 24 hours at 40 °C specimens (JANNuS#1 and JANNuS#2). The deuterium profile obtained in the heat-treated reference material is added for comparison.

Figure 9 : Normalized (to ^{52Cr} signal in bulk) SIMS ^{2H} profiles on reference (red line) and JANNuS#2 implanted (blue squares) specimens after 500 h oxidation in heavy primary water (11.8 MPa, 320 °C). The ^{2H} SIMS profile obtained after cathodic charging (black diamonds) at room temperature is recalled. Note that here the SIMS signals are represented according to a Log scale.

Figure 10 : Comparison between the simulated depth profile (using Fick's second law and taking into account the history of charging and aging) with the experimental deuterium profile obtained on the heat-treated reference specimen. Simulation was performed with optimized D0 and ED values.

Figure 11 : Effective implantation defects distribution profiles obtained from TEM measurements, after transformation a) of Frank loop density and size into an equivalent linear dislocation density, and b) of cavity density and size into a partial volume fraction of cavities. Both implantation sets defects profiles are represented: JANNuS#1 in red circles, JANNuS#2 in blue squares.

Figure 12 : Direct comparison of normalized deuterium concentration profiles obtained by SIMS (black curve) and by simulations (blue squares) taking into account Frank dislocations loops only as trap sites for hydrogen: a) JANNuS#2 and b) JANNuS#1 implantation sets.

Figure 13 : Direct comparison of normalized deuterium concentration profiles obtained by SIMS (black curve) and by simulations (blue squares) taking into account the cavities only as trap sites for hydrogen: a) JANNuS#2 and b) JANNuS#1 implantation sets. Insert in b) zooms in the 0-2 µm area from surface.

Figure 14 : Quantified deuterium distribution at voids for JANNuS#1 specimen (right, black dotted line) and for JANNuS#2 specimen (left, blue line) within the first 1600 nm from the surface.

Table captions

Table 1 : Nominal composition of the industrial 316L SS in wt.% obtained by Optical Emission Spectrometry

Table 2 : List of the boundary conditions corresponding to the experimental history of the specimens used for the simulation of the final deuterium concentration profiles obtained in SIMS.

Table 3 : Trapping (k) and detrapping (p) kinetic constants for trapping at dislocations in A600 nickel-based alloy [39]; these values were used in the present study for the 316L austenitic stainless steel.